

Iron Isotopes Constrain Sub-Seafloor Hydrothermal Processes at the TAG Active Sulfide Mound, 26°N Mid-Atlantic Ridge

Fredrik Sahlström (✉ fredrik.sahlstrom@uit.no)

UiT The Arctic University of Norway <https://orcid.org/0000-0003-2677-6571>

Valentin Troll

Uppsala University <https://orcid.org/0000-0003-1891-3396>

Sabina Strmić Palinkaš

UiT The Arctic University of Norway

Ellen Kooijman

Swedish Museum of Natural History

Xin-Yuan Zheng

University of Minnesota – Twin Cities

Article

Keywords:

Posted Date: February 25th, 2022

DOI: <https://doi.org/10.21203/rs.3.rs-1338313/v1>

License:  This work is licensed under a Creative Commons Attribution 4.0 International License.

[Read Full License](#)

Version of Record: A version of this preprint was published at Communications Earth & Environment on August 29th, 2022. See the published version at <https://doi.org/10.1038/s43247-022-00518-2>.

Abstract

Sub-seafloor hydrothermal processes along volcanically active plate boundaries are integral to the formation of seafloor massive sulfide (SMS) deposits and to oceanic Fe cycling, yet their nature is poorly understood. Here we apply Fe isotope analysis to sulfides from the TAG mound and underlying stockwork, 26°N Mid-Atlantic Ridge, to trace hydrothermal processes inside an actively-forming SMS deposit in a sediment-free mid-ocean ridge setting. We show that data for recently formed chalcopyrite imply fluid–mound interactions cause small negative shifts (< -0.1‰) to the $\delta^{56}\text{Fe}$ signature of dissolved Fe released from TAG into the North Atlantic Ocean. Texturally resolved pyrite, in turn, preserves a $\delta^{56}\text{Fe}$ range from -1.27 to +0.56‰ that reflects contrasting modes of formation (fluid–seawater mixing vs. fluid conductive cooling) and variable degrees of progressive hydrothermal maturation during the >20 kyr evolution of the TAG complex. The identified processes may explain Fe isotope variations found in fossil onshore sulfide deposits.

Introduction

Seafloor massive sulfide (SMS) deposits form as part of high-temperature submarine hydrothermal systems that are driven by volcanism along both divergent and convergent plate boundaries^{1–3}. They are a potential future source of metals deemed critical for technology and industry (e.g., Cu, Zn and Au)⁴ and represent modern analogs to volcanogenic massive sulfide (VMS) deposits currently exploited in ancient volcanic successions onshore⁵. In addition, hydrothermal venting atop active SMS deposits creates a unique biological habitat that is proposed to have supported early life on Earth^{6,7} and fluxes a wide range of chemicals from the oceanic crust into the oceans. In this context, it is increasingly recognized that hydrothermal vents are significant contributors to the oceanic inventory of dissolved Fe, a key micronutrient that regulates phytoplankton growth and hence the biological ‘carbon pump’^{8–13}.

SMS genesis is considered to involve (1) exhalative sulfide deposition, forming chimney and mound structures at the seafloor, and (2) sub-seafloor infilling and replacement of primary hydrothermal precipitates and volcanic material by sulfide^{5,14–18}. Sub-seafloor mineralization in particular is shown to be key in producing large-tonnage sulfide deposits, yet the nature of the hydrothermal processes involved remains poorly constrained^{5,15,16,18}. Since evidence for such processes is commonly obscured by geologic overprinting in fossil (obducted) onshore VMS deposits, ocean drilling of active SMS systems represents a crucial source of information for detailed characterization of sub-seafloor hydrothermal activity in a range of tectonic settings^{18–22}. To this end, stable Fe isotopes in sulfides from the internal portions of an active SMS deposit offer a novel method to further elucidate such processes, including their role in the oceanic biogeochemical cycling of Fe²³. Moreover, such *in-situ* sub-seafloor Fe isotope data have the potential to help reconcile existing Fe isotope observations from hydrothermal vents and plumes atop active SMS systems with those from fossil onshore VMS deposits and from experimental studies of high-temperature hydrothermal sulfide formation^{8,13,24–34}, which would significantly broaden the applicability of this method.

Here, we apply Fe isotope analysis of sulfide minerals to a suite of historical drill cores from the Trans-Atlantic Geotraverse (TAG) active mound and stockwork complex of the north-central Mid-Atlantic Ridge (Fig. 1). The TAG complex formed through intermittent cycles of high-temperature hydrothermal activity over at least the last 20,000 years^{35–37} and its detailed growth history includes repeated hydrothermal precipitation at and below the mound surface, mechanical and hydrothermal reworking of earlier formed precipitates, and progressive alteration and partial assimilation of the basaltic host rocks to the complex^{15,19,38,39}. Building on this geologic and hydrothermal framework, we use our new sulfide Fe isotope data to further constrain sub-seafloor hydrothermal processes at TAG and assess their implications for ore formation and for Fe cycling in the North Atlantic Ocean. The unique insights gathered from our study of TAG will likely enhance the utility of Fe isotopes to the investigation of active and fossil seafloor hydrothermal systems elsewhere.

The TAG mound and stockwork complex. The TAG active sulfide mound was discovered in 1985⁴⁰ at the E margin of the rift valley of the slow-spreading Mid-Atlantic Ridge at 26°N (Fig. 1) and is located in an area featuring several relict sulfide and oxide deposits^{41–43}. Following its discovery, TAG was the first-ever SMS deposit investigated by the Ocean Drilling Program (ODP) in 1994^{44,45} and it is now one of the World's most comprehensively characterized seafloor hydrothermal systems. The mound is located about 2.5 km E of the neovolcanic zone of the ridge at ~ 3670 m water depth. It forms a distinctly circular structure composed of two superposed terraces, and it measures ~ 200 m in basal diameter and rises ~ 50 m above the seafloor^{19,46} (Fig. 1b). The mound is underlain by a ~ 80 m diameter, pipe-shaped stockwork of mineralized and intensely altered basaltic basement rocks that extends to at least 125 m below the surface^{19,38} (Fig. 2a). The mound and underlying stockwork are estimated to contain a combined volume of ~ 3.9 million tonnes of sulfide with an average grade of 1–2% Cu. The morphology, size and bulk composition of TAG is comparable to that of some of the largest-known VMS deposits preserved in ophiolites, e.g., those exploited in Cyprus, in Oman and in Newfoundland⁴⁷.

Presently, high-temperature (360–370°C), Cu-rich black smoker fluids are discharged from a cluster of chalcopyrite-pyrite-anhydrite chimneys situated on top of a ~ 20 m diameter cone structure in the NW part of the upper terrace (the 'Black Smoker Complex'; Figs. 1b and 2a)^{48–50}. A field of sphalerite-dominated, beehive-shaped chimneys occurs on the lower terrace ~ 70 m SE of the Black Smoker Complex and is named the 'Kremlin Area' (Figs. 1b and 2a). Prior to and during ODP drilling, these chimneys vented white smoker fluids that were distinctly colder (260–300°C) and were Cu-Fe-poor, but Zn-rich relative to the black smoker discharges. These white smokers were suggested to have evolved from an end-member black smoker fluid via conductive cooling and mixing with entrained seawater within the mound^{48–50}. The white smoker venting was however observed to have ceased during revisits in 2003 and later⁵¹.

The mound surface is made up entirely of hydrothermal precipitates including plate-like crusts and bulbous blocks of porous massive sulfide as well as siliceous Fe-oxyhydroxide sediments. Oxidized sulfide talus and debris flows form an apron that surrounds and partially covers the steep-sided margins of the mound⁴⁸. Below the surface, the upper part of the mound (0 to ~ 15 m.b.s.f.) consists of a thin

layer of Fe-oxyhydroxides and chert that overlies massive pyrite and massive pyrite breccias with locally significant amounts of chalcopyrite, sphalerite and marcasite^{15,19,39,44,52} (Fig. 2a). The massive pyrite zone is underlain by an anhydrite-rich zone made up of pyrite-anhydrite and pyrite-silica(-anhydrite) breccias that extends down to ~ 45 m.b.s.f. (Fig. 2a). The breccias in this zone are extensively crosscut by up to ~ 45 cm thick, composite anhydrite veins with localized sulfide mineralization⁵³. The pyrite-silica(-anhydrite) breccias at the base of the anhydrite-rich zone define the transition from the mound to the upper part of the stockwork, which comprises pyrite-silica breccias that grade into silicified wallrock breccias with depth³⁹ (Fig. 2a). Below ~ 100 m.b.s.f., the silicified wallrock breccias eventually transition into chloritized basalt breccias that are overprinted by multiple generations of pyrite, quartz, and quartz-pyrite stringer veins¹⁹ (Fig. 2a).

Results

Iron isotope compositions were determined for a total of 50 micro-drilled sulfide separates encompassing the main rock types from the vertical and lateral extent of the TAG mound and the underlying stockwork (Fig. 2a). The TAG sulfides show an overall range of $\delta^{56}\text{Fe}$ values between -1.27 and +0.56‰, with a mean value of +0.04‰ ($\pm 0.08\text{‰}, 2\sigma$; Table 1, Supplementary Table 1). Notably, variations in $\delta^{56}\text{Fe}$ values are observed between the different textural types of sulfide analyzed, including (following ref. 53): (1) massive sulfide; (2) vein-related sulfide; (3) sulfide in clasts from different breccia types; and (4) disseminated sulfide in altered basalt host rock.

Table 1
Summary of Fe isotope data for TAG sulfides.

Sample type	Mineral	n	Mean $\delta^{56}\text{Fe}$ (‰) ^a	Mean 2σ	Minimum $\delta^{56}\text{Fe}$ (‰) ^a	Maximum $\delta^{56}\text{Fe}$ (‰) ^a
Overall	Pyrite, Chalcopyrite	50	0.04	0.08	-1.27	0.56
Massive sulfide	Pyrite	9	-0.42	0.08	-1.27	0.28
Sulfide in anhydrite veins	Pyrite	5	-0.24	0.07	-0.52	0.06
Sulfide in anhydrite veins	Chalcopyrite	3	0.01	0.07	-0.04	0.08
Sulfide in quartz-pyrite stringer veins	Pyrite	3	0.22	0.07	0.09	0.38
Sulfide in breccia clasts	Pyrite	22	0.12	0.09	-0.32	0.37
Disseminated sulfide in altered basalt host rock	Pyrite	8	0.47	0.07	0.34	0.56

^a $\delta^{56}\text{Fe}$ corresponds to $^{56}\text{Fe}/^{54}\text{Fe}$ ratio relative to IRMM-14 international standard.

Massive sulfide. Massive sulfide (sulfide-only) samples from the upper portions of the TAG mound are dominated by fine-grained, variably porous pyrite that in places preserves primary colloform and spheroidal textures¹⁵ (Fig. 2b). Similar variably porous massive sulfide occurs locally also as cement in silicified wallrock breccias at deeper levels. Pyrite from massive sulfide samples shows a mean $\delta^{56}\text{Fe}$ value of -0.42‰ and a range from -1.27 to +0.28‰ (n = 9; Table 1, Supplementary Table 1).

Vein-related sulfide. The anhydrite vein networks within the pyrite-anhydrite and pyrite-silica(-anhydrite) zones contain sulfides locally. Fine-grained pyrite and chalcopyrite are aggregated in bands or clots within the veins (Fig. 2c), with more voluminous sulfide present in selvages and halos along the vein margins^{15,19,53}. Pyrite samples from the anhydrite veins and selvages show $\delta^{56}\text{Fe}$ values between -0.52 and +0.06‰ with a mean of -0.24‰ (n = 5), whereas co-existing chalcopyrite records $\delta^{56}\text{Fe}$ values between -0.04 and +0.08‰ with a mean of +0.01‰ (n = 3; Table 1, Supplementary Table 1).

Coarse-grained pyrite from quartz-pyrite stringer veins crosscutting the chloritized basalt breccias in the deeper parts of the TAG stockwork (Fig. 2e) shows $\delta^{56}\text{Fe}$ values between +0.09 and +0.38‰ with a mean of +0.22‰ (n = 3; Table 1, Supplementary Table 1).

Sulfide in breccia clasts. Clasts of massive sulfide occur throughout the pyrite, pyrite-anhydrite, pyrite-silica(-anhydrite), and the pyrite-silica breccias at TAG (Fig. 2d). The breccia clasts range from a few mm up to >5 cm in diameter and are chiefly made up of compact, granular aggregates of polycrystalline euhedral pyrite¹⁵. Some sulfide clasts, however, contain fine-grained microporous domains that preserve remains of colloform and spheroidal mineral textures, whereas some other clasts exhibit sequential growth banding¹⁵. Locally preserved microcrystalline pyrite textures are also noted and may represent a precursor to some coarser pyrite clasts¹⁵. Pyrite from the breccia clasts exhibits $\delta^{56}\text{Fe}$ values between -0.32 and +0.37‰ with a mean of +0.12‰ (n = 22; Table 1, Supplementary Table 1).

Disseminated sulfide in altered basalt host rock. The finely disseminated pyrite samples extracted from within variably altered basalt fragments in the silicified wallrock and chloritized basalt breccias of the TAG complex (Fig. 2e) yield a mean $\delta^{56}\text{Fe}$ value of +0.47‰ and show a range from +0.34 to +0.56‰ (n = 8; Table 1, Supplementary Table 1).

Discussion

Assessment of fluid Fe isotope fractionation within the TAG mound. In a typical mid-ocean ridge setting, the Fe content and isotopic composition of the hydrothermal fluid is initially set during high-temperature leaching and alteration of basalt in the reaction zone. This process is suggested to enrich the fluid in Fe that is isotopically light (^{56}Fe -depleted) relative to MORB ($\delta^{56}\text{Fe}_{\text{MORB}} \approx +0.1\text{\textperthousand}$)^{23,25,54–56}. Upon entering and migrating through a large sulfide mound such as TAG, the fluid will be progressively modified through mineral precipitation in open spaces as well as reworking of pre-existing hydrothermal precipitates along its path to the seafloor^{14,57}. However, it remains unclear in how far fluid Fe isotope

compositions are affected (fractionated) during such interaction^{24–26}. Experimental studies have indicated that chalcopyrite formed in seafloor hydrothermal systems rapidly achieves Fe isotopic equilibrium with the co-existing fluid and hence chalcopyrite $\delta^{56}\text{Fe}$ values can be used to assess fluid compositions³¹. Utilizing the fractionation factor provided by ref. 31 (i.e., $\Delta^{56}\text{Fe}_{\text{chalcopyrite-Fe(aq)}} = 0.09 \pm 0.17\text{\textperthousand}$, 2σ), three vein-related chalcopyrite samples from the lower part of the TAG mound (30 to 50 m.b.s.f.) yield equilibrium fluid $\delta^{56}\text{Fe}$ values of -0.13 to -0.01‰ ($\pm 0.18\text{\textperthousand}$, 2σ ; Supplementary Table 1), which are about 0.1 to 0.25‰ lower than MORB values^{23,56}. The range of our inferred $\delta^{56}\text{Fe}_{\text{fluid}}$ values overlaps with and extends to slightly higher values relative to recently (1998) measured vent fluids from the Black Smoker Complex (-0.17 to -0.11 $\pm 0.02\text{\textperthousand}$, 2σ)²⁸. Since anhydrite within the TAG mound dissolves during inactive periods, the preservation of anhydrite in the chalcopyrite-bearing veins indicates that they formed during the current high-temperature hydrothermal cycle that commenced at approximately 100 years ago^{37,39,58,59}. Our inferred and the measured²⁸ fluid datasets can thus be interpreted in conjunction and imply that recent TAG hydrothermal fluids experience small negative shifts in their $\delta^{56}\text{Fe}$ values (< -0.1‰) during ascent through the mound to the black smoker vent site, which we chiefly attribute to hydrothermal maturation of pyritic sulfides (discussed further below). Following venting, oxidation of Fe^{2+} and precipitation of Fe-oxyhydroxides within the TAG hydrothermal plume cause a more extensive decrease in the $\delta^{56}\text{Fe}$ values of dissolved Fe, down to -1.35‰^{13,32}. This final volume of dissolved Fe with low $\delta^{56}\text{Fe}$ values has been observed to then travel in seawater via currents up to thousands of kilometres away from the TAG site, likely influencing surface planktonic activity in the North Atlantic Ocean¹³. Our results now allow us to track the isotopic evolution of dissolved Fe throughout the TAG hydrothermal system and reveal an overall and stepwise decrease in $\delta^{56}\text{Fe}$ values. This finding expands our knowledge on the sequence of (bio-)geochemical processes that contribute to the Fe isotopic signature of hydrothermally sourced Fe^{8,24–29,32,54} and will thereby help to further refine identification and quantification of such Fe in the global oceans and in associated sedimentary records^{8,13,60}.

Evolution of sub-seafloor mineralization at TAG constrained by pyrite $\delta^{56}\text{Fe}$ values. Based on the $\delta^{56}\text{Fe}_{\text{fluid}}$ values from ref. 28 and those calculated in this study, combined with the Fe isotope fractionation factors of ref. 30 and ref. 34, the range of $\delta^{56}\text{Fe}$ values of pyrite in equilibrium with recent TAG hydrothermal fluids is expected to be +0.45 to +1.32‰ (including the 2σ uncertainty; Fig. 3). Notably, only a small subset of our pyrite data plot within this range (6 out of 47; Fig. 3, Supplementary Table 1). However, unlike chalcopyrite, formation of pyrite in seafloor hydrothermal systems has been proposed to occur via transient precursor mineral species that may impose significant kinetic effects on Fe isotope fractionation^{26,30,34,61,62}. On the basis of a synthesis of available experimental and theoretical data, ref. 34 proposed a two-stage model for the formation and Fe isotopic equilibration of hydrothermal pyrite at high temperature ($> 300^\circ\text{C}$). In this model, a rapid (few days) initial stage of pyrite formation occurs via an aqueous Fe (poly)sulfide precursor phase whose detailed nature (stoichiometry, coordination and magnetic spin) depends on the fluid composition. This short-lived Fe (poly)sulfide

precursor obtains Fe isotopic equilibrium with the hydrothermal fluid, and its $\delta^{56}\text{Fe}$ signature is then transferred without fractionation upon conversion to pyrite. The initial pyrite will thereby be out of Fe isotopic equilibrium with the hydrothermal fluid and will have a $\delta^{56}\text{Fe}$ value that may be up to $\sim 1.5\text{\textperthousand}$ lower than the value expected for pyrite in equilibrium with the fluid ($\Delta^{56}\text{Fe}_{\text{pyrite-Fe(aq)}} \approx 0.8\text{--}1\text{\textperthousand}$ at 300–450°C)^{30,34}. The $\delta^{56}\text{Fe}_{\text{pyrite}}$ value will then gradually increase toward this equilibrium value during a subsequent and much slower stage of pyrite recrystallization and Fe isotopic equilibration with the fluid^{30,34}. Rates of ≥ 1 year to reach pyrite–fluid Fe isotopic equilibrium have been estimated under ideal (experimental) conditions³⁴, although it is not yet clear what timescales apply to the progressive hydrothermal maturation of pyrite commonly observed in natural SMS and VMS systems^{52,63}. Here we attempt to shed further light on this issue and integrate our texturally resolved pyrite Fe isotope dataset into a refined geologic and hydrothermal framework of TAG^{15,19,35–39,52}.

The lowest $\delta^{56}\text{Fe}_{\text{pyrite}}$ values at TAG are found in the massive sulfide mineralization concentrated in the upper parts of the mound (Fig. 3, Table 1). These values are distinctly lower than the estimated $\delta^{56}\text{Fe}$ values of pyrite in equilibrium with TAG fluids (Fig. 3) and they partly overlap with $\delta^{56}\text{Fe}_{\text{pyrite}}$ values reported from seafloor sulfide chimneys elsewhere^{25,26}. The most negative $\delta^{56}\text{Fe}_{\text{pyrite}}$ values in our sample suite reach down to $-1.27\text{\textperthousand}$ and correspond to porous massive sulfide samples from TAG-4 that exhibit well-developed colloform textures (Fig. 2b). The preservation of such primary depositional features in the massive sulfide and its ‘chimney-like’ pyrite Fe isotope signature are consistent with recent formation at or near the mound surface by growth into open space¹⁵. Here, mixing between high-temperature hydrothermal fluid and cold seawater likely led to rapid precipitation of pyrite with kinetically-driven low $\delta^{56}\text{Fe}$ values (i.e., strong pyrite–fluid disequilibrium), which have not yet been extensively modified by later hydrothermal maturation (Fig. 3).

Exploring this phenomenon in more detail, we find that pyrite samples from the anhydrite veins in the lower part of the TAG mound (Fig. 2c) have low $\delta^{56}\text{Fe}$ values that overlap the values for massive sulfide (Fig. 3, Table 1). Notably, the majority of these $\delta^{56}\text{Fe}_{\text{pyrite}}$ values are lower than the $\delta^{56}\text{Fe}$ values of co-existing chalcopyrite from the veins. This confirms significant Fe isotopic disequilibrium in this pyrite group, since pyrite should have higher $\delta^{56}\text{Fe}$ values than those of chalcopyrite if in isotopic equilibrium ($\Delta^{56}\text{Fe}_{\text{pyrite-chalcopyrite}} \approx 0.9\text{\textperthousand}$ at 350°C)³¹. The presence of anhydrite suggests that the veins formed recently (≤ 100 years ago³⁷, see above) due to mixing between hydrothermal fluid and entrained seawater within the mound⁵⁹. Similar to the massive sulfide, the low $\delta^{56}\text{Fe}_{\text{pyrite}}$ values of the anhydrite veins can thus be explained by rapid pyrite precipitation followed by only very limited hydrothermal maturation and Fe isotopic equilibration with later fluids (Fig. 3). On the other hand, the coarser-grained pyrite from quartz-pyrite stringer veins in the TAG stockwork (Fig. 2e) have distinctly higher $\delta^{56}\text{Fe}$ values than those of pyrite from the anhydrite veins (Fig. 3, Table 1). These data are consistent with the deep quartz-pyrite stringer veins having formed due to conductive cooling of the hydrothermal fluid rather than as a result of mixing with seawater, such that the rates of pyrite precipitation were slower and greater Fe

isotopic equilibration between pyrite and the fluid could occur^{26,34,59}. Furthermore, crosscutting relationships confirm that the quartz-pyrite stringer veins are older than the anhydrite veins⁵³ and have thus likely been subjected to more extensive hydrothermal maturation, leading to further increase in the $\delta^{56}\text{Fe}_{\text{pyrite}}$ values^{30,34} (Fig. 3).

Pyrite in the sulfide clasts that occur in the different breccia types (Fig. 2d) show $\delta^{56}\text{Fe}$ values that are overall higher than, but in part overlap the $\delta^{56}\text{Fe}_{\text{pyrite}}$ values of the massive sulfide and the anhydrite veins. The values are similar to the $\delta^{56}\text{Fe}_{\text{pyrite}}$ values of the quartz-pyrite stringer veins, but are always lower than the estimated $\delta^{56}\text{Fe}$ values of pyrite in equilibrium with the TAG hydrothermal fluids (Fig. 3, Table 1). Pyrite in these clasts likely have diverse and possibly complex origins that involve combinations of recrystallization and reworking of surficial (massive) and vein-related mineralization as well as in-situ nucleation and growth of new pyrite¹⁵. Such heterogeneous pyrite assemblages should initially have $\delta^{56}\text{Fe}$ values similar to those of the massive and the vein-related pyrite described above, but the $\delta^{56}\text{Fe}_{\text{pyrite}}$ values will progressively shift to higher values as a result of variable degrees of hydrothermal maturation during the protracted development of the TAG breccias, thus offering a sensible explanation for the observed data spread in this particular sample group (Fig. 3).

Remarkably, the finely disseminated pyrite preserved within remnant fragments of altered basalt (Fig. 2e) has the highest $\delta^{56}\text{Fe}$ values observed at TAG, showing only minor overlap with $\delta^{56}\text{Fe}_{\text{pyrite}}$ values of the quartz-pyrite stringer veins and the sulfide breccia clasts (Fig. 3, Table 1). Within individual core samples, disseminated pyrite always has distinctly higher $\delta^{56}\text{Fe}$ values than those of pyrite that texturally overprints the altered basalt clasts (e.g., stringer veins or massive sulfide cement; Fig. 3). High-temperature hydrothermal alteration of the basaltic basement rocks would have commenced during the initial stages of the evolution of TAG and involves chloritization followed by progressive paragonitization and silicification of the basalt, with pyrite forming throughout the alteration sequence^{38,39}. Clasts of such variably altered basalt do not only occur in the TAG stockwork, but have also been incorporated into the mound breccias at depths much shallower than that expected for the top of the basement. The reason for this is poorly understood, but could potentially be related to processes akin to 'frost jacking and heaving' during repeated expansion (due to internal anhydrite precipitation) and collapse (anhydrite dissolution) of the TAG mound over several high-temperature hydrothermal cycles^{15,38}. Disseminated pyrite preserved in the basalt clasts may thus represent the most extensively reworked sulfide sample material of this study. Such hydrothermal maturation appears to occur intermittently over tens of thousands of years during which the basaltic basement is progressively altered and assimilated into the TAG breccias^{15,37–39}, imparting a characteristic isotope signature of $\delta^{56}\text{Fe}_{\text{pyrite}}$ values in near-equilibrium to equilibrium with the hydrothermal fluids (Fig. 3).

In summary, we interpret the observed range of $\delta^{56}\text{Fe}$ values for different textural types of pyrite to reflect contrasting modes of formation (fluid–seawater mixing vs. fluid conductive cooling) and variable degrees of progressive hydrothermal maturation during the evolution of the TAG mound and stockwork

complex (Fig. 3). In contrast to the idealized rates suggested from experiments (≥ 1 year to reach pyrite–fluid equilibrium³⁴), our results suggest that Fe isotopic equilibration during hydrothermal maturation of pyrite occurs over timescales of tens of thousands of years within large and periodically inactive SMS deposits such as TAG, allowing the preservation of the $\delta^{56}\text{Fe}_{\text{pyrite}}$ variations that we observe. The observed Fe isotope variations further imply that the W part of the TAG mound (TAG-4) has experienced less extensive hydrothermal maturation than the other parts, consistent with the mineralogical and geochemical asymmetry noted during the original ODP investigation⁵². Importantly, similar processes can probably explain Fe isotope variations in sulfides from fossil onshore VMS deposits (e.g., immature, low- $\delta^{56}\text{Fe}$ ‘black ores’ and mature, high- $\delta^{56}\text{Fe}$ ‘yellow ores’), such as the ones found in the classic Kuroko deposits of Japan³³. Our study of TAG therefore concludes that sulfide Fe isotope compositions can provide detailed insight into the nature, longevity and dynamics of hydrothermal processes in SMS deposits and allow us to create a valuable reference framework for future investigation of similar active and fossil hydrothermal systems elsewhere.

Methods

Sampling. Sub-seafloor samples from the TAG mound and stockwork were sourced from five drill cores (957C, 957E, 957H, 957M and 957P) originally collected onboard R/V *JOIDES Resolution* during ODP Leg 158, September–November 1994⁴⁴ (Fig. 1b). Sulfide mineral separates, generally 10 to 100 mg, were extracted from cm-sized drill core pieces using a small-diameter electric drill. Petrographic examination aided the selection of monomineralic sampling sites; in a few cases however, the fine intergrowths of sulfides only allowed for the recovery of mixtures (pyrite-chalcopyrite or pyrite-marcasite; Supplementary Table 1). The drill tip was repeatedly dipped into ethanol and cleaned using Kimwipes and compressed air between each sample extraction to avoid cross-contamination.

Iron isotope analysis. Iron isotope compositions of sulfide separates ($n = 50$) were determined at the Vegacenter at the Swedish Museum of Natural History in Stockholm. First, Fe-bearing clays and silicates, variably present in separates from altered basalt ($n = 8$), were removed by dissolution in 10M HF acid at room temperature for three days followed by centrifugation and rinsing of the residue with MilliQ-water. Complete removal of clays and silicates was then confirmed via powder X-ray diffraction (XRD) analysis using the instrumentation and protocol described in ref. 64. The leached and unleached sulfide separates were then dissolved and purified for Fe isotope analysis following a procedure adapted from ref. 65 and previously used in ref. 66. About 15 mg of each sample was weighed and transferred to 7 ml Perfluoroalkoxy alkane vials. A volume of 1.5 ml 8M HNO₃ was then added to each sample after which they were evaporated on a hotplate at 70°C. Once dry, 0.75 ml concentrated HNO₃ and 0.5 ml 6M HCl were added before evaporating the samples again. The evaporated residues were subsequently dissolved in 0.3M HNO₃. For Fe separation, aliquots of these solutions (each assumed to contain 200–300 µg Fe) were transferred to clean vials and diluted ten times with de-ionized water to obtain 0.03M HNO₃. Purification was then done by anion exchange chromatography using 100–200 mesh AGMP-1M resin.

After Fe separation, the samples were dried and then converted to nitric form by repeated dissolution in concentrated HNO₃. The samples were finally dissolved in 5 ml 0.3M HNO₃ prior to Fe isotope analysis.

Iron isotope analysis was done using an Aridus II Nebulizer system coupled to a Nu Plasma II HR-MC-ICP-MS operated in medium-resolution mode (50 µm slit width, resolving power ~ 7000). This setup resulted in a sensitivity of ~ 6–9 V/ppm for δ⁵⁶Fe for solutions measured at 2 ppm Fe. The sample uptake rate was ~ 100 µL/min resulting in ~ 500 µL sample consumption per analysis. The instrumental Fe background was 30–40 mV for δ⁵⁶Fe (~ 0.2–0.3% of sample intensity) based on on-mass zero measurements of pure 0.3M HNO₃ at the beginning of each run. Each sample was measured six times in a row. The analyses were corrected for mass bias by standard–sample bracketing using the IRMM-014 international standard. Results are reported as δ⁵⁶Fe and δ⁵⁷Fe, which correspond to the deviations of ⁵⁶Fe/⁵⁴Fe and ⁵⁷Fe/⁵⁴Fe relative to IRMM-014 in per mil (Supplementary Table 1). The external reproducibility was 0.07‰ for δ⁵⁶Fe and 0.10‰ for δ⁵⁷Fe (2σ), based on repeated measurements of the Alfa Aesar standard solution⁶⁷ as an unknown throughout the analytical session. Data for samples and standards plot along a mass-dependent fractionation line in a δ⁵⁶Fe vs. δ⁵⁷Fe diagram (Supplementary Fig. 1), confirming that isobaric interferences were properly corrected for. Only δ⁵⁶Fe_{IRMM-014} values are discussed in the manuscript and figures and all cited literature data have been converted to the same scale.

Declarations

Data availability

The authors declare that all relevant data are available within the article and its supplementary information files.

Acknowledgements

The authors would like to thank Karin Wallner and Melanie Kielman-Schmitt for assistance during Fe isotope analysis at Vegacenter. Keiko Hattori, Jeff Hedenquist and Antonio Arribas gave helpful advice on sample preparation methods. We further thank the International Ocean Discovery Program (IODP) for providing the TAG drill core samples. Generous funding from Equinor and the Swedish Research Council (VR) is gratefully acknowledged. This is Vegacenter publication #xxx.

Author contributions

F.S., S.S.P. and V.R.T. conceived the study. Micro-sampling was carried out by F.S. and Fe isotope analysis was performed by E.K. at Vegacenter. Data interpretation and manuscript preparation was carried out by F.S. with contributions from all co-authors.

Competing interests: The authors declare no competing interests.

References

1. Corliss, J. B. et al. Submarine thermal springs on the Galapagos Rift. *Science* **203**, 1073–1083 (1979).
2. Rona, P. A. Hydrothermal mineralization at seafloor spreading centers. *Earth-Sci. Rev.* **20**, 1–104 (1984).
3. Hannington, M. D., de Ronde, C. E. J. & Petersen, S. Sea-floor tectonics and submarine hydrothermal systems. In: *Economic Geology One Hundredth Anniversary Volume* (eds. Hedenquist, J. W. et al.) 111–141 (Society of Economic Geologists, 2005).
4. Lustig, P. A. J. & Murton, B. J. Deep-ocean mineral deposits: metal resources and windows into earth processes. *Elements* **14**, 301–306 (2018).
5. Franklin, J. M., Gibson, H. L., Jonasson, I. R. & Galley, A. G. Volcanogenic massive sulfide deposits. In: *Economic Geology One Hundredth Anniversary Volume* (eds. Hedenquist, J. W. et al.) 523–560 (Society of Economic Geologists, 2005).
6. Martin, W., Baross, J., Kelley, D. & Russell, M. J. Hydrothermal vents and the origin of life. *Nat. Rev. Microbiol.* **6**, 805–814 (2008).
7. Dodd, M. S. et al. Evidence for early life in Earth's oldest hydrothermal vent precipitates. *Nature* **543**, 60–64 (2017).
8. Beard, B. L., Johnson, C. M., Von Damm, K. L. & Poulsen, R. L. Iron isotope constraints on Fe cycling and mass balance in oxygenated Earth oceans. *Geology* **31**, 629–632 (2003).
9. Bennett, S. A. et al. The distribution and stabilisation of dissolved Fe in deep-sea hydrothermal plumes. *Earth Planet. Sci. Lett.* **270**, 157–167 (2008).
10. Tagliabue, A. et al. Hydrothermal contribution to the oceanic dissolved iron inventory. *Nat. Geosci.* **3**, 252–256 (2010).
11. Sander, S. G. & Koschinsky, A. Metal flux from hydrothermal vents increased by organic complexation. *Nat. Geosci.* **4**, 145–150 (2011).
12. Saito, M. A. et al. Slow-spreading submarine ridges in the South Atlantic as a significant oceanic iron source. *Nat. Geosci.* **6**, 775–779 (2013).
13. Conway, T. & John, S. Quantification of dissolved iron sources to the North Atlantic Ocean. *Nature* **511**, 212–215 (2014).
14. Hannington, M. D., Jonasson, I. R., Herzig, P. M. & Petersen, S. Physical and chemical processes of seafloor mineralization at mid-ocean ridges. In: *Seafloor Hydrothermal Systems: Physical, Chemical, Biological, and Geological Interactions*, *Geophys. Monogr. Ser.* **91** (eds. Humphris, S. E. et al.) 115–157 (American Geophysical Union, 1995).
15. Knott, R., Fouquet, Y., Honnorez, J., Petersen, S. & Bohn, M. Petrology of hydrothermal mineralization: a vertical section through the TAG mound. In: *Proc. ODP. Sci. Results* **158** (eds. Herzig, P. M. et al.) 5–26 (Ocean Drilling Program, 1998).

16. Doyle, M. G. & Allen, R. L. Subsea-floor replacement in volcanic-hosted massive sulfide deposits. *Ore Geol. Rev.***23**, 183–222 (2003).
17. Piercy, S. J. A semipermeable interface model for the genesis of subseafloor replacement-type volcanogenic massive sulfide (VMS) deposits. *Econ. Geol.***110**, 1655–1660 (2015).
18. Nozaki, T. et al. Subseafloor sulphide deposit formed by pumice replacement mineralisation. *Sci. Rep.***11**, 8809 (2021).
19. Humphris, S. E. et al. The internal structure of an active sea-floor massive sulphide deposit. *Nature***377**, 713–716 (1995).
20. Zierenberg, R. A. et al. The deep structure of a sea-floor hydrothermal deposit. *Nature***392**, 485–488 (1998).
21. Barriga, F. J. A. S., Binns, R. A., Miller, D. J. & Herzig, P. M. (eds.) *Proc. ODP. Sci. Results 193* (Ocean Drilling Program, 2007).
22. de Ronde, C. E. J., Humphris, S. E., Höfig, T. W., Reyes, A. G. & the IODP Expedition 376 Scientists. Critical role of caldera collapse in the formation of seafloor mineralization: the case for Brothers volcano. *Geology***47**, 762–766 (2019).
23. Johnson, C. M., Beard, B. L. & Weyer, S. Iron geochemistry: an isotopic perspective (Springer, 2020).
24. Sharma, M., Polizzotto, M. & Anbar, A. Iron isotopes in hot springs along the Juan de Fuca Ridge. *Earth Planet. Sci. Lett.***194**, 39–51 (2001).
25. Rouxel, O., Fouquet, Y. & Ludden, J. N. Subsurface processes at the Lucky Strike hydrothermal field, Mid-Atlantic Ridge: evidence from sulfur, selenium, and iron isotopes. *Geochim. Cosmochim. Acta***68**, 2295–2311 (2004).
26. Rouxel, O., Shanks III, W. C., Bach, W. & Edwards, K. J. Integrated Fe- and S-isotope study of seafloor hydrothermal vents at East Pacific Rise 9–10°N. *Chem. Geol.***252**, 214–227 (2008).
27. Rouxel, O., Toner, B. M., Manganini, S. J. & German, C. R. Geochemistry and iron isotope systematics of hydrothermal plume fall-out at East Pacific Rise 9°50'N. *Chem. Geol.***441**, 212–234 (2016).
28. Severmann, S. et al. The effect of plume processes on the Fe isotope composition of hydrothermally derived Fe in the deep ocean as inferred from the Rainbow vent site, Mid-Atlantic Ridge, 36°14'N. *Earth Planet. Sci. Lett.***225**, 63–76 (2004).
29. Bennett, S. A. et al. Iron isotope fractionation in a buoyant hydrothermal plume, 5°S Mid-Atlantic Ridge. *Geochim. Cosmochim. Acta***73**, 5619–5634 (2009).
30. Syverson, D. D., Borrok, D. M. & Seyfried Jr, W. E. Experimental determination of equilibrium Fe isotopic fractionation between pyrite and dissolved Fe under hydrothermal conditions. *Geochim. Cosmochim. Acta***122**, 170–183 (2013).
31. Syverson, D. D. et al. Fe isotope fractionation between chalcopyrite and dissolved Fe during hydrothermal recrystallization: an experimental study at 350 °C and 500 bars. *Geochim. Cosmochim. Acta***200**, 87–109 (2017).

32. Revels, B. N., Ohnemus, D. C., Lam, P. J., Conway, T. M. & John, S. G. The isotopic signature and distribution of particulate iron in the North Atlantic Ocean. *Deep Sea Res. Part II Top. Stud. Oceanogr.* **116**, 321–331 (2015).
33. Otake, T. et al. Large Fe isotope fractionations in sulfide ores and ferruginous sedimentary rocks from the Kuroko volcanogenic massive sulfide deposits in the Hokuroku district, northeast Japan. *Geochim. Cosmochim. Acta* **295**, 49–64 (2021).
34. Pokrovski, G. S., Blanchard, M., Saunier, G. & Poitrasson, F. Mechanisms and rates of pyrite formation from hydrothermal fluid revealed by iron isotopes. *Geochim. Cosmochim. Acta* **304**, 281–304 (2021).
35. Lalou, C. et al. Geochronology of TAG and Snakepit hydrothermal fields, Mid-Atlantic Ridge: witness to a long and complex hydrothermal history. *Earth Planet. Sci. Lett.* **97**, 113–128 (1990).
36. Lalou, C. et al. New age data for Mid-Atlantic Ridge hydrothermal sites: TAG and Snakepit chronology revisited. *J. Geophys. Res. Solid Earth* **98**, 9705–9713 (1993).
37. Lalou, C., Reyss, J. L. & Brichet, E. Age of sub-bottom sulfide samples at the TAG active mound. In: *Proc. ODP. Sci. Results 158* (eds. Herzig, P. M. et al.) 111–117 (Ocean Drilling Program, 1998).
38. Honnorez, J. J., Alt, J. C. & Humphris, S. E. Vivisection and autopsy of active and fossil hydrothermal alterations of basalt beneath and within the TAG hydrothermal mound. In: *Proc. ODP. Sci. Results 158* (eds. Herzig, P. M. et al.) 231–254 (Ocean Drilling Program, 1998).
39. Petersen, S., Herzig, P. & Hannington, M. D. Third dimension of a presently forming VMS deposit: TAG hydrothermal mound, Mid-Atlantic Ridge, 26°N. *Miner. Depos.* **35**, 233–259 (2000).
40. Rona, P. A., Klinkhammer, G., Nelsen, T. A., Trefry, J. H. & Elderfield, H. Black smokers, massive sulphides and vent biota at the Mid-Atlantic Ridge. *Nature* **321**, 33–37 (1986).
41. Thompson, G., Mottl, M. J. & Rona, P. A. Morphology, mineralogy, and chemistry of hydrothermal deposits from the TAG area, 26°N Mid-Atlantic Ridge. *Chem. Geol.* **49**, 243–257 (1985).
42. Rona, P. A. et al. Active and relict sea-floor hydrothermal mineralization at the TAG hydrothermal field, Mid-Atlantic Ridge. *Econ. Geol.* **88**, 1989–2017 (1993).
43. Gruber, S. et al. Structural control, evolution, and accumulation rates of massive sulfides in the TAG hydrothermal field. *Geochem. Geophys. Geosystems* **21**, e2020GC009185 (2020).
44. Humphris, S. E. et al. (1996) *Proc. ODP. Init. Repts. 158* (Ocean Drilling Program, 1996).
45. Herzig, P. M., Humphris, S. E., Miller, D. J., & Zierenberg, R. A. (eds.) *Proc. ODP. Sci. Results 158* (Ocean Drilling Program, 1998).
46. Humphris, S. E. & Kleinrock, M. C. Detailed morphology of the TAG active hydrothermal mound: insights into its formation and growth. *Geophys. Res. Lett.* **23**, 3443–3446 (1996).
47. Hannington, M. D., Galley, A. G., Herzig, P. M. & Petersen, S. (1998) Comparison of the TAG mound and stockwork complex with Cyprus-type massive sulfide deposits. In: *Proc. ODP. Sci. Results 158* (eds. Herzig, P. M. et al.) 389–415 (Ocean Drilling Program, 1998).
48. Tivey, M. K., Humphris, S. E., Thompson, G., Hannington, M. D. & Rona, P. A. Deducing patterns of fluid flow and mixing within the TAG active hydrothermal mound using mineralogical and

- geochemical data. *J. Geophys. Res. Solid Earth***100**, 12527–12555 (1995).
49. Edmond, J. M. et al. Time series studies of vent fluids from the TAG and MARK sites (1986, 1990) Mid-Atlantic Ridge: a new solution chemistry model and a mechanism for Cu/Zn zonation in massive sulphide orebodies. *Geol. Soc. Spec. Publ.***87**, 77–86 (1995).
50. Edmonds, H. N. et al. Continuation of the hydrothermal fluid chemistry time series at TAG, and the effects of ODP drilling. *Geophys. Res. Lett.***23**, 3487–3489 (1996).
51. Sohn, R. A. Stochastic analysis of exit fluid temperature records from the active TAG hydrothermal mound (Mid-Atlantic Ridge, 26°N): 1. Modes of variability and implications for subsurface flow. *J. Geophys. Res. Solid Earth***112**, B07101 (2007).
52. Fouquet, Y., Henry, K., Knott, R. & Cambon, P. Geochemical section of the TAG hydrothermal mound. In: *Proc. ODP Sci. Results 158* (eds. Herzig, P. M. et al.) 363–387 (Ocean Drilling Program, 1998).
53. Gemmell, J. B. & Sharpe, R. Detailed sulfur-isotope investigation of the TAG hydrothermal mound and stockwork zone, 26°N, Mid-Atlantic Ridge. In: *Proc. ODP Sci. Results 158* (eds. Herzig, P. M. et al.) 71–84 (Ocean Drilling Program, 1998).
54. Rouxel, O., Dobbek, N., Ludden, J. & Fouquet, Y. Iron isotope fractionation during oceanic crust alteration. *Chem. Geol.***202**, 155–182 (2003).
55. Chapman, J. B., Weiss, D. J., Shan, Y. & Lemberger, M. Iron isotope fractionation during leaching of granite and basalt by hydrochloric and oxalic acids. *Geochim. Cosmochim. Acta***73**, 1312–1324 (2009).
56. Teng, F. -Z., Dauphas, N., Huang, S. & Marty, B. Iron isotopic systematics of oceanic basalts. *Geochim. Cosmochim. Acta***107**, 12–26 (2013).
57. Janecky, D. R. & Shanks, W. C. Computational modeling of chemical and sulfur isotopic reaction processes in seafloor hydrothermal systems: chimneys, massive sulfides, and subjacent alteration zones. *Can. Mineral.***26**, 805–826 (1988).
58. Blouinot, C. W. & Dickson, F. W. The solubility of anhydrite (CaSO_4) in $\text{NaCl-H}_2\text{O}$ from 100 to 450°C and 1 to 1000 bars. *Geochim. Cosmochim. Acta***33**, 227–245 (1969).
59. Brügmann, G. E., Birck, J. L., Herzig, P. M. & Hofmann, A. W. Os isotopic composition and Os and Re distribution in the active mound of the TAG hydrothermal system, Mid-Atlantic Ridge. In: *Proc. ODP Sci. Results 158* (eds. Herzig, P. M. et al.) 91–100 (Ocean Drilling Program, 1998).
60. Zhu, X. K., O'Nions, R. K., Guo, Y. & Reynolds, B. C. Secular variation of iron isotopes in North Atlantic deep water. *Science***287**, 2000–2002 (2000).
61. Butler, I. B., Archer, C., Vance, D., Oldroyd, A. & Rickard, D. Fe isotope fractionation on FeS formation in ambient aqueous solution. *Earth Planet. Sci. Lett.***236**, 430–442 (2005).
62. Polyakov, V. B. & Soultanov, D. M. New data on equilibrium iron isotope fractionation among sulfides: constraints on mechanisms of sulfide formation in hydrothermal and igneous systems. *Geochim. Cosmochim. Acta***75**, 1957–1974 (2011).

63. Velasco-Acebes, J. et al. Isotope geochemistry tracks the maturation of submarine massive sulfide mounds (Iberian Pyrite Belt). *Miner. Depos.***54**, 913–934 (2019).
64. Sahlström, F. et al. Interaction between high-temperature magmatic fluids and limestone explains ‘Bastnäs-type’ REE deposits in central Sweden. *Sci. Rep.***9**, 15203 (2019).
65. Craddock, P. R., Rouxel, O. J., Ball, L. A. & Bach, W. Sulfur isotope measurement of sulfate and sulfide by high-resolution MC-ICP-MS. *Chem. Geol.***253**, 102–113 (2008).
66. Troll, V. R. et al. Global Fe–O isotope correlation reveals magmatic origin of Kiruna-type apatite-iron-oxide ores. *Nat. Commun.***10**, 1712 (2019).
67. Fehr, M. A., Andersson, P. S., Hålenius, U. & Mört, C. -M. Iron isotope variations in Holocene sediments of the Gotland Deep, Baltic Sea. *Geochim. Cosmochim. Acta***72**, 807–826 (2008).
68. Ryan, W. B. F. et al. Global multi-resolution topography synthesis. *Geochem. Geophys. Geosystems***10**, Q03014 (2009).
69. Grant, H. L. J., Hannington, M. D., Petersen, S., Frische, M. & Fuchs, S. H. Constraints on the behavior of trace elements in the actively-forming TAG deposit, Mid-Atlantic Ridge, based on LA-ICP-MS analyses of pyrite. *Chem. Geol.***498**, 45–71 (2018).
70. Roman, C. & Singh, H. A self-consistent bathymetric mapping algorithm. *J. Field Robot.***24**, 23–50 (2007).
71. Tivey, M. K., Mills, R. A. & Teagle, D. A. Temperature and salinity of fluid inclusions in anhydrite as indicators of seawater entrainment and heating in the TAG active mound. In: *Proc. ODP. Sci. Results* 158 (eds. Herzig, P. M. et al.) 179–190 (Ocean Drilling Program, 1998).

Figures

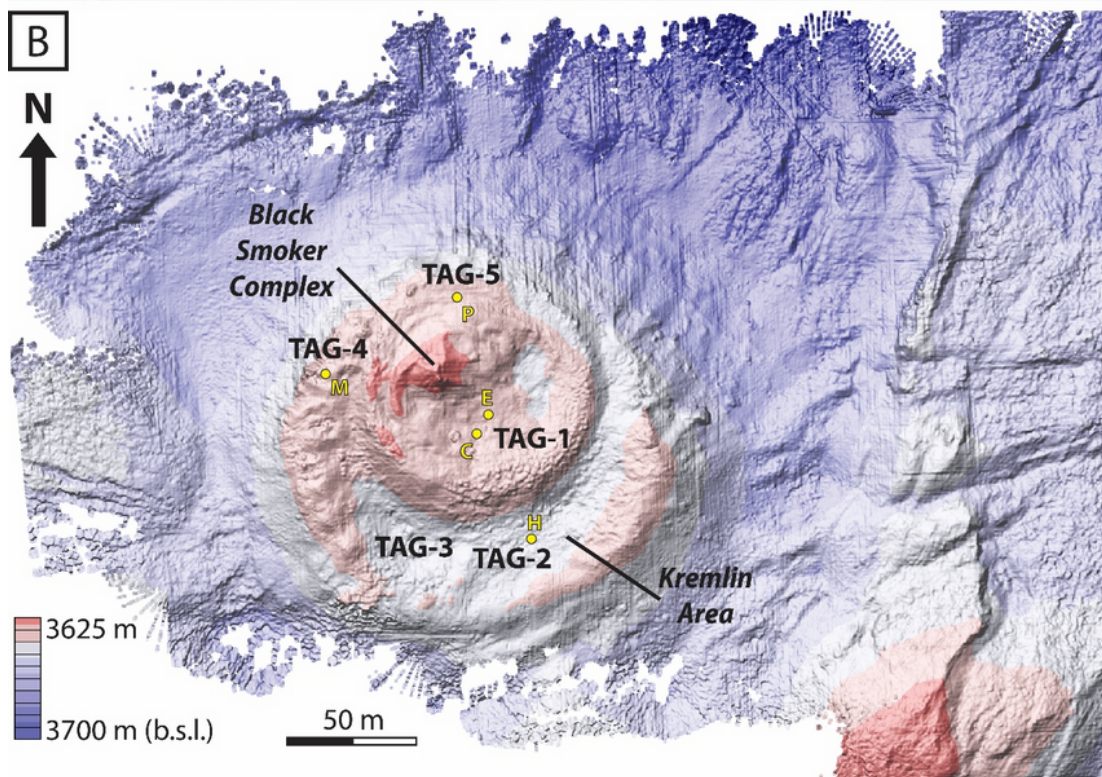
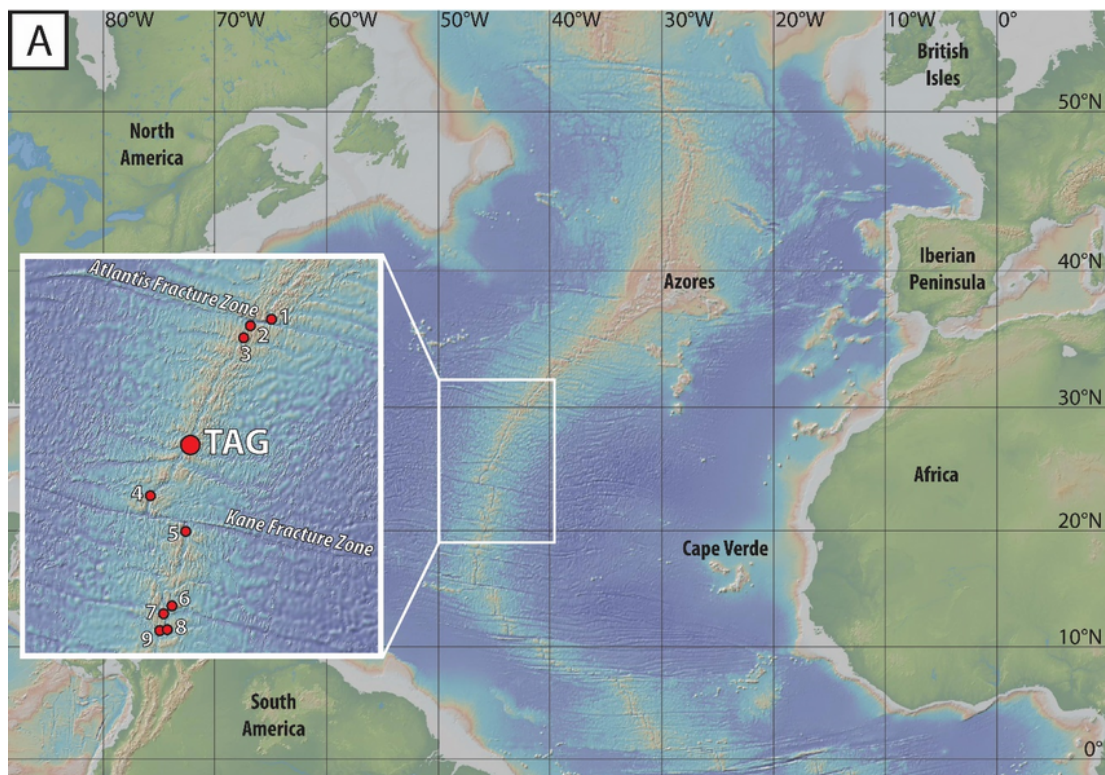


Figure 1

Bathymetric maps with sampling locations. **(A)** Location of TAG and other hydrothermal vent fields and sulfide deposits (red symbols) along the TAG segment, north-central Mid-Atlantic Ridge: 1 – Lost City; 2 – MAR 30°N; 3 – Broken Spur; 4 – MAR 24°30'N; 5 – Snakepit; 6 – Surprise; 7 – Puy des Folles; 8 – Zenith-Victory; 9 – Yubileinoe. Modified from ref. 68 and ref. 69. **(B)** Detailed map of the TAG mound showing

the collar locations of the ODP Leg 158 drill cores used in this study (957C, 957E, 957H, 957M and 957P). Modified from ref. 70.

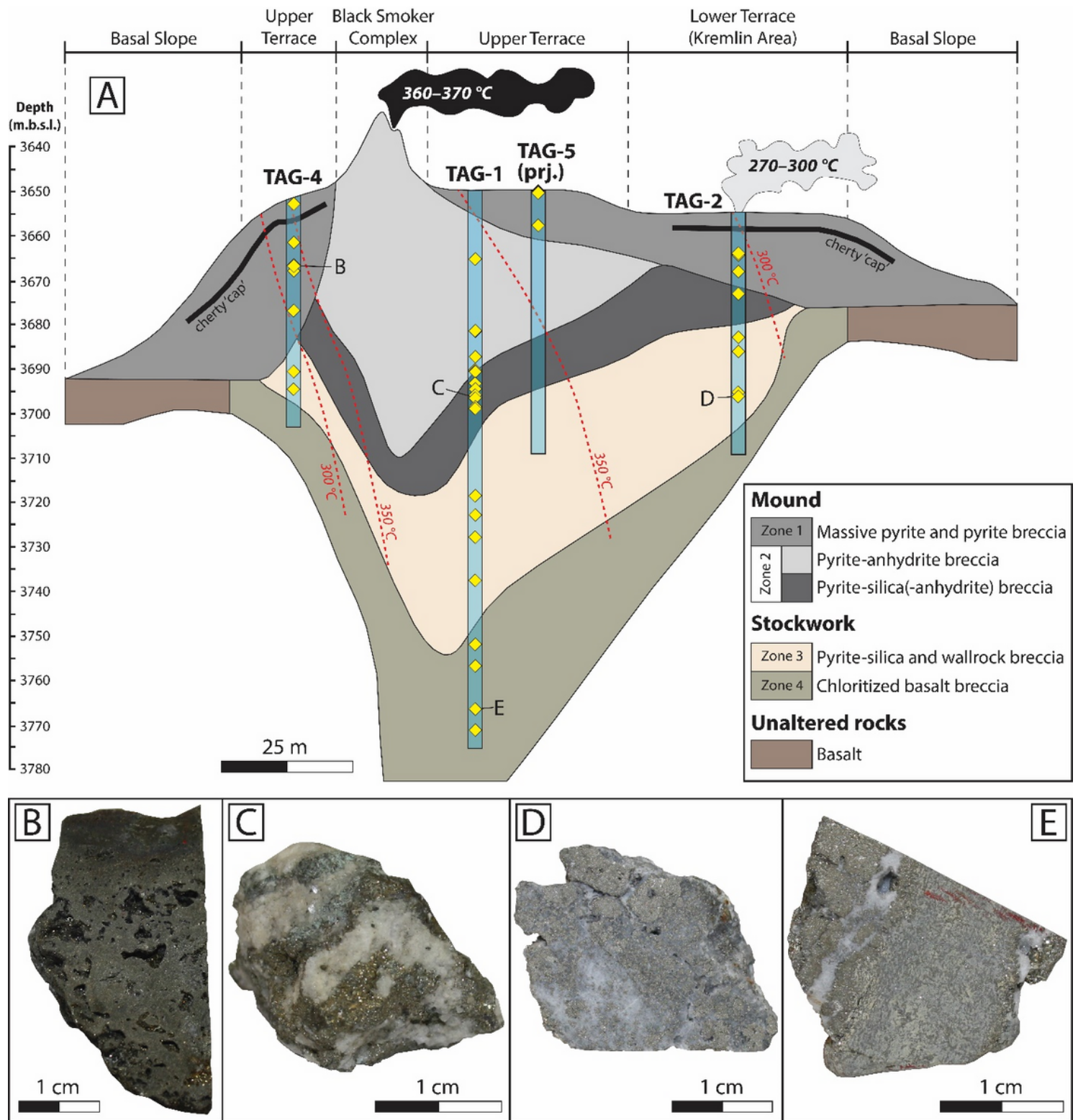


Figure 2

Internal structure of TAG and examples of sampled sulfide textures. **(A)** Composite section through the TAG mound and underlying stockwork drawn based on multiple drill cores in each area; TAG-5 is projected onto the section. The samples utilized in this study (yellow diamonds) encompass the main rock types from the vertical and lateral extent of TAG^{19,44}: massive pyrite and pyrite breccia (types 5 and 6); pyrite-anhydrite breccia (type 7) and pyrite-silica(-anhydrite) breccia (type 8), both with abundant anhydrite veins (type 11); pyrite-silica and silicified wallrock breccia (types 9 and 10a); and chloritized basalt breccia (type 10b). Vent fluid temperatures for the Black Smoker Complex and the (now inactive) Kremlin Area are from ref. 49 and isotherms are drawn based on fluid inclusion data^{39,71}. Modified from ref. 52 and ref. 69. **(B)** Massive sulfide mineralization from the upper parts of the mound comprising fine-grained and porous pyrite and marcasite with local chalcopyrite. The top part of the rock piece preserves a colloform texture (TAG-4, 957M, 14.79 m.b.s.f.). **(C)** Aggregates of pyrite and chalcopyrite (partly oxidized, greenish in photo) within a fragment of an anhydrite vein from the lower part of the mound (TAG-1, 957C, 46.69 m.b.s.f.). **(D)** Pyrite-silica breccia from the upper part of the stockwork comprising clasts of massive granular pyrite in a matrix of quartz and pyrite (TAG-2, 957H, 41.32 m.b.s.f.). **(E)** Fragment of chloritized basalt host rock with finely disseminated pyrite from the deeper part of the stockwork. The altered basalt is crosscut by quartz-pyrite stringer veins (TAG-1, 957E, 116.42 m.b.s.f.).

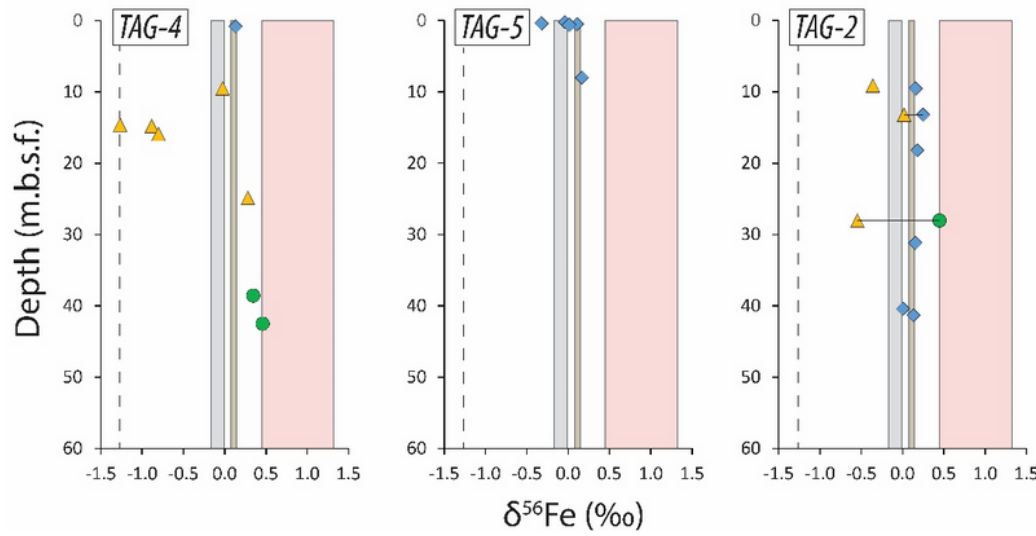
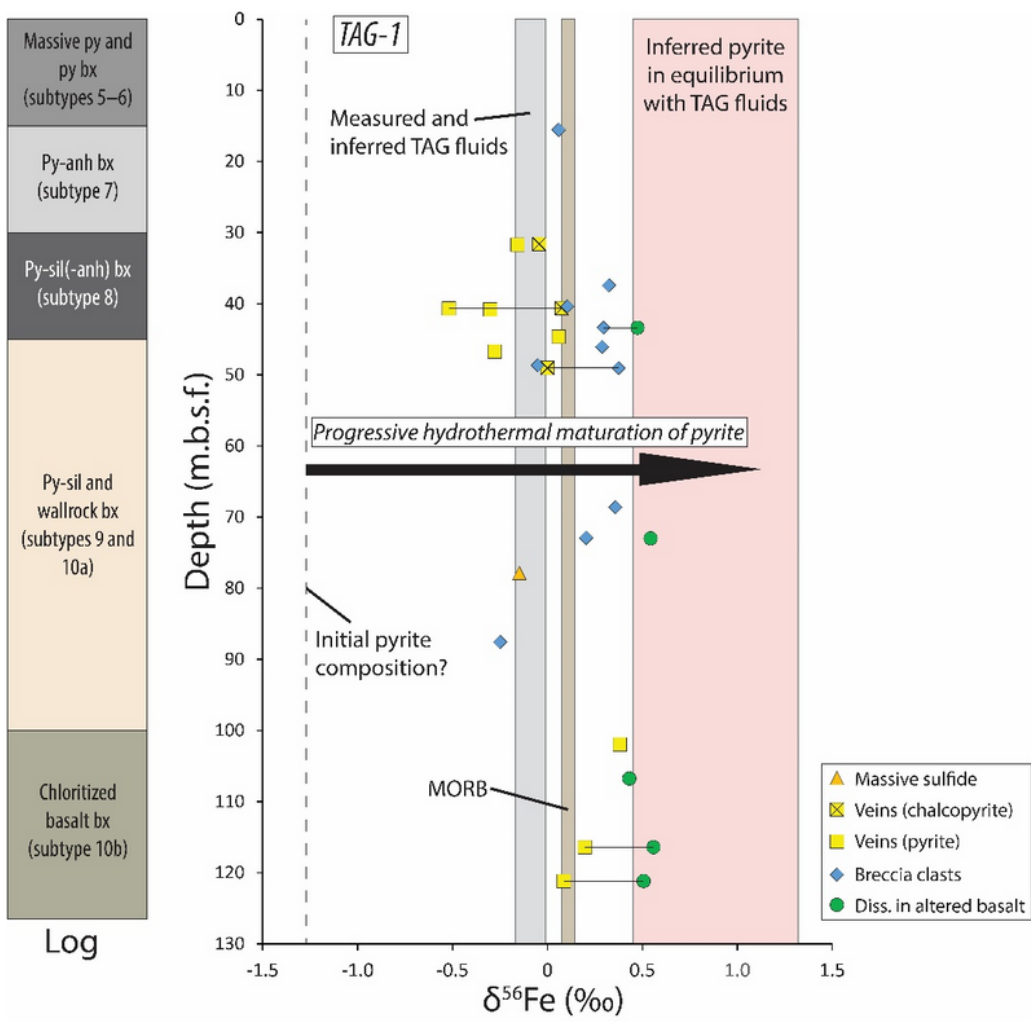


Figure 3

Plots of $\delta^{56}\text{Fe}$ values of pyrite ($n = 47$) and chalcopyrite ($n = 3$) from TAG-1, TAG-2, TAG-4 and TAG-5, respectively, as a function of depth below the mound surface. Tie-lines connect sulfide samples obtained from the same drill core piece. Included are the core log for TAG-1⁴⁴ and reference fields for MORB (brown)^{23,56} and for measured and inferred TAG hydrothermal fluids (grey; ref. 28; this study). The

inferred range of $\delta^{56}\text{Fe}$ values of pyrite in equilibrium with recent TAG fluids (pink) was calculated using the fractionation factors of ref. 30 and ref. 34. The lowest $\delta^{56}\text{Fe}_{\text{pyrite}}$ value of our dataset (-1.27 ‰; TAG-4) is used to illustrate a potential initial (disequilibrium) Fe isotope composition of pyrite formed via Fe (poly)sulfide precursors (dashed black line; cf. ref. 34). We interpret the observed range of $\delta^{56}\text{Fe}$ values of different textural types of pyrite to reflect contrasting modes of formation (fluid–seawater mixing vs. fluid conductive cooling) and variable degrees of progressive hydrothermal maturation during the evolution of the TAG complex. See text for details. Abbreviations: anh – anhydrite; bx – breccia; diss. – disseminated; py – pyrite; sil – silica.

Supplementary Files

This is a list of supplementary files associated with this preprint. Click to download.

- [Supplementarydata.xlsx](#)